THE JOURNAL OF PHYSICAL CHEMISTRY C
A JOURNAL OF THE AMERICAN CHEMICAL SOCIETY

pubs.acs.org/JPCC
Article

Exploring Light Harvesting in Blends of Cesium Lead Halide Nanocrystals with Fullerene Derivatives

Eleftheria Charalambous, Paris G. Papagiorgis, Nefeli Polycarpou, Fedros Galatopoulos, Apostolos Ioakeimidis, Stelios Choulis, Sotirios Christodoulou, and Grigorios Itskos*

Cite This: J. Phys. Chem. C 2024, 128, 5947−5955

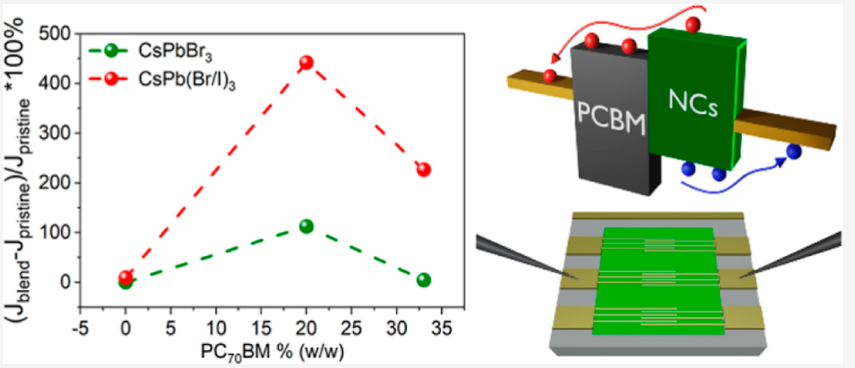

ABSTRACT: Light harvesting devices based on metal halide perovskite nanocrystals (NCs) rely on the application of ligand washing or ligand exchange processes to transform pristine, glassy NC solids into electronically active NC arrays. A less explored route combines such treatments with the fabrication of NC heterojunctions with organic semiconductors to promote charge transfer through conductive pathways within the blends. Herein, optical spectroscopy and photoconductivity is implemented for a detailed investigation of the charge generation and charge extraction process in blends of green $CsPbBr_3$ NCs or red $CsPb(Br,I)_3$ NCs capped with short octylamine/octanoic-acid ligands with the fullerene derivative phenyl-C_{70}-butyric acid methyl ester ($PC_{70}BM$). Incorporation of the fullerene results in efficient quenching of the NC photoluminescence (PL) and the emergence of a fast subnanosecond decay channel in the transient PL, which is consistent with efficient interfacial dissociation of the NC excitons via electron transfer to the $PC_{70}BM$. Importantly, the photocurrent in lateral devices with gold contacts is improved by up to 2 orders of magnitude upon fullerene incorporation, with optimum concentration of 20% per weight $PC_{70}BM$ for both green and red absorbing NCs. Short, post synthetic thermal annealing up to 100 °C further improves charge extraction due to better material blending and film quality, increasing by an additional order of magnitude the photo response of the devices.

INTRODUCTION

Lead halide perovskite nanocrystals (LHP NCs) emerged as highly promising classical and quantum emitters with excellent prospects for applications in displays, solid-state lighting, optically pumped lasers, single photon sources, scintillators etc.[1−3] Notable progress has also been achieved in LHP NC light harvesting devices, such as solar cells, even though efficiencies are below the state-of-the-art reported for polycrystalline perovskite photovoltaics. Nanostructured perovskites, especially in the form of colloidal NCs, exhibit however some favorable properties compared to their bulk analogues that include an overall better stability of the 3-D perovskite photoactive phase owing to the protective ligand shell as well as improved band gap engineering due to the implementation of compositional tuning and dielectric and quantum confinement effects.[1−3] Novel phenomena observed in perovskites, such as hot carrier cooling[4,5] and multiexciton generation,[6] also appear to be reinforced by confinement, being potentially exploitable for future perovskite NC-based light-harvesting. On the solar cell development, initial encouraging results were obtained in $CsPbI_3$ NC-based devices produced via postsynthetic removal of the native insulating ligands and build-up of the active region via layer-by-layer assembly.[7] Further improvement relied on the addition of cation halide salts to passivate defects formed by the ligand desorption[8] and the implementation of graded heterostructures, homojunctions, and multinary NC compositions,[9−12]

Received: November 26, 2023
Revised: March 15, 2024
Accepted: March 15, 2024
Published: April 2, 2024

allowing to reach power conversion efficiencies at a level of 17%.[11] In parallel to such devices relying on purely NC active regions, alternative approaches have started to emerge that include the implementation of heterojunctions with organic electronic conductors. In such blends, efficient NC exciton quenching and charge extraction can be mediated by appropriate design of heterointerfaces and segregation of the NC and organic components within the blends. Based on this concept, high-performance solar cells and photodetectors were recently developed using binary or ternary combinations of LHP NCs with fullerenes and conjugated polymers acting as electron or hole acceptors.[13−18] The most common n-type materials employed in those demonstrations are fullerene derivatives such as phenyl-C_{60}-butyric acid methyl ester ($PC_{60}BM$), and phenyl-C_{70}-butyric acid methyl ester ($PC_{70}BM$). PCBM-based molecules have been employed successfully as electron acceptors, transporters, interlayers, and buffer layers in organic and bulk perovskite PVs. In LHP NC-based devices, $PC_{60}BM$ and $PC_{70}BM$ have been shown to act as excellent quenchers for inorganic Cs-based and hybrid FA-based NC excitons,[13−15,17] mediating fast exciton dissociation, electron extraction, and transport while functioning also as adhesives and additives improving mechanical flexibility[15] and passivating defects and interfaces.[15,18]

Herein, we report on a systematic investigation based on luminescent techniques and lateral photoconductive devices to provide further insight into the exciton dissociation, charge transport and collection processes in blends of green-emitting $CsPbBr_3$ or red-emitting mixed halide $CsPb(Br,I)_3$ NCs with $PC_{70}BM$. A simple synthesis is implemented allowing the fabrication of perovskite NCs decorated by short octylamine and octanoic-acid ligands[19] combined with a mild film postdeposition washing of excess ligands and synthesis byproducts. The octylamine/octanoic-acid ligands provide efficient surface NC passivation while allowing improved electronic NC−NC and NC-$PC_{70}BM$ coupling, resulting in increased charge transfer, charge extraction, and photocurrent generation. Notably, all the synthesis, film deposition, and annealing processing steps are performed in ambient conditions with the exemption of a final slow drying step of the produced films, carried out in vacuum.

EXPERIMENTAL SECTION

Material Synthesis. $CsPbBr_3$ NCs capped with octylamine octanoic acid ligands were synthesized following the precipitation technique reported in ref 19. $CsPb(Br/I)_3$ NCs were fabricated by performing an anion exchange reaction to freshly synthesized $CsPbBr_3$ NCs, following the procedure described in ref 20. The NC solutions were produced at a concentration of 100−120 mg/ml. $PC_{70}BM$ was diluted in toluene, forming a solution of 60 mg/mL and treated via an ultrasonic bath for at least 20 min to suppress extended fullerene aggregation.

Film Deposition. All films were fabricated in ambient conditions *o*n 1 × 1 cm^2 quartz substrates. The substrates were cleaned by boiling the substrates in *N*-butyl acetate at 300 °C. They were subsequently placed in acetone, sonicated for at least 20 min, and finally washed and stored in *i*-propanol. An amount of ∼80 μL solution in toluene of pristine NCs or a mix of NCs and $PC_{70}BM$ of the desired mass relative concentration (w/w) ratio was deposited on the substrates via spin-coating at 1500 rpm for 40 s, followed by a drying step of 4000 rpm for 20 s. To obtain sufficiently conductive NC films, a mild washing of excess ligands and synthesis byproducts was achieved by covering the films with a lead acetate solution created by diluting $Pb(NO_3)_2$ in EtAc[7] and subsequent spin-coating at 1500 rpm for 60 s. The deposition process was repeated two times to obtain two stacked layer films, based on the optical and device optimization studies, as contained in Figure S1. All samples were stored overnight in vacuum to complete the drying process. For the thermal annealing study, the samples were placed on a hotplate and annealed for a short period of 5 min at the desired temperature.

Device Fabrication. Lateral photoconductive devices were fabricated via the two stacked NC-$PC_{70}BM$ layer deposition procedure described above, on interdigitated Au electrodes with a channel length of ∼50 μm. The electrodes were fabricated via thermal evaporation of ∼150 nm thick and 50 μm wide Au layers using an Ossila E323 shadow mask, as visualized in the optical microscopy images in Figure S2. Films and devices are coded based on their NC type [G: $CsPbBr_3$, R: $CsPb(Br,I)_3$] and relative $PC_{70}BM$ w/w content (0, 20, and 33%); the asterisk refers to reference NC samples that are not imposed to the postdeposition lead acetate solution washing. The sample list is given in Table 1.

Table 1. Samples under Study, with Code Names Used in the Manuscript

Sample	NC type	$PC_{70}BM$ w/w (%)
G1*	$CsPbBr_3$	0
G1		0
G2		20
G3		33
R1*	$CsPb(Br,I)_3$	0
R1		0
R2		20
R3		33

Optical Spectroscopy. Optical absorption spectra were obtained by a Perkin Elmer, Lambda 1050 spectrophotometer. Steady-state photoluminescence (PL) was recorded on a 0.35 m FluoroLog FL3 Horiba Jobin Yvon spectrofluorometer equipped with a visible TBX-04 PMT. The samples were excited via a monochromator-filtered, 450 W ozone-free Xe lamp at 405 nm. The acquired PL spectra were normalized to the absorbance of each film at the excitation wavelength. The normalization was performed to account for the different sample content and film thickness variations, allowing direct comparison of the emission intensity in the studied films (PL quenching experiments). The same spectrophotometer was used for time-resolved PL measurements based on time-correlated single-photon counting. A 405 nm laser diode with a pulse width of ∼80 ps was used for the sample excitation. The decays were monitored at the PL peak with a spectral bandwidth of ∼5 nm.

Device Characterization. Photoconductivity was carried out on a custom-made setup composed of a modified epifluorescence microscope and a Keithley 2461 source meter. The devices were placed on the microscope stage and excited with a 405 nm cw laser diode, operating at a maximum power of 32 mW. Light from the excitation source illuminated the device's active region through the objective lens of the microscope. Initially, a voltage of 3 V was applied by the Keithley source meter through electrode tips that contact the device's Au electrodes. The *I*−*V* curves were collected in the

https://doi.org/10.1021/acs.jpcc.3c07761
J. Phys. Chem. C 2024, 128, 5947−5955

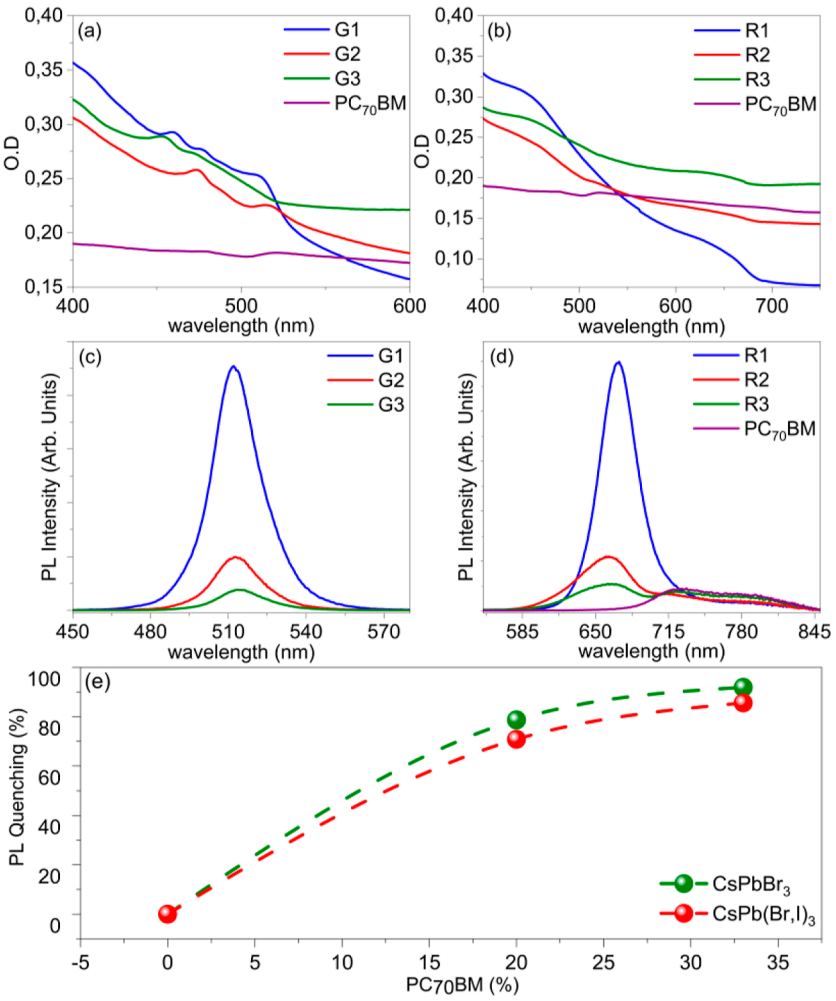

Figure 1. Optical density spectra of (a) $CsPbBr_3$ NC-based, (b) $CsPb(Br,I)_3$ NC-based samples; the purple curve shows the extinction spectra of a reference drop-casted $PC_{70}BM$ film. (c,d) Comparative steady-state PL of the $CsPbBr_3$ NC- and $CsPb(Br,I)_3$ NC-based blends, respectively. (e) PL quenching values of the samples as a function of relative fullerene content.

range of −3 to +3 V under a laser bias to record the photoconductivity data. The 405 nm excitation power was normalized to the 405 nm absorbance of each sample and divided by the excited area of the device to calculate the photocurrent density. The photocurrent density was calculated by estimating the conductive channel cross section as the product of the average film thickness of ∼150 nm, times the width of ∼18 mm per each channel. The current density is then obtained by the ratio of the measured current over the calculated channel cross section.

RESULTS AND DISCUSSION

Optical density and steady-state PL spectra of the studied films containing green- and red-emitting NCs and the corresponding blends with $PC_{70}BM$ are displayed in Figure 1. The energy of the ground-state NC excitonic absorption is around ∼512 nm and ∼655 nm for the $CsPbBr_3$ and $CsPb(Br,I)_3$ NCs, respectively. As the fullerene content increases, the NC exciton weakens and sub-gap extinction increases. The increase is attributed to absorption and light scattering by fullerene aggregates. Clustering of the $PC_{70}BM$ molecules has been commonly observed in the solid state with its extent being dependent on various parameters that include material concentration, solvent type, film deposition, and postdeposition conditions.[21] In the case of our samples, extended $PC_{70}BM$ aggregation was found to inhibit photocurrent generation and was suppressed by ultrasonic cleaning of the solution prior to film deposition. However, a significant fraction of smaller aggregates was still present in the films, contributing to the subgap extinction, as hinted by the similarity in the spectra of the blends with the spectrum obtained by the aggregated pristine $PC_{70}BM$ film. Small-scale clustering and phase-separating domains of NCs and fullerenes can be beneficial to charge extraction and collection, as shown by various studies on organic and hybrid electronic material blends.[21,22]

Incorporation of the fullerene acceptor resulted in efficient suppression of the NC luminescence in both $CsPbBr_3$ (G2, G3) and $CsPb(Br,I)_3$ (R2, R3) NC-based blends. The PL quenching is quantified by eq 1

$$\text{PL quenching} = \frac{\text{PL}_{\text{pristine}} - \text{PL}_{\text{blend}}}{\text{PL}_{\text{pristine}}} \times 100\% \quad (1)$$

with $\text{PL}_{\text{pistine}}$, PL_{blend} being the integrated PL intensity of the pristine and the blend films, respectively, when the excitation intensity is normalized to the absorbance of each film, as elaborated on the Experimental Section. The PL spectra are dominated by the NC emission, peaked at 512 nm and 670 nm

https://doi.org/10.1021/acs.jpcc.3c07761
J. Phys. Chem. C 2024, 128, 5947−5955

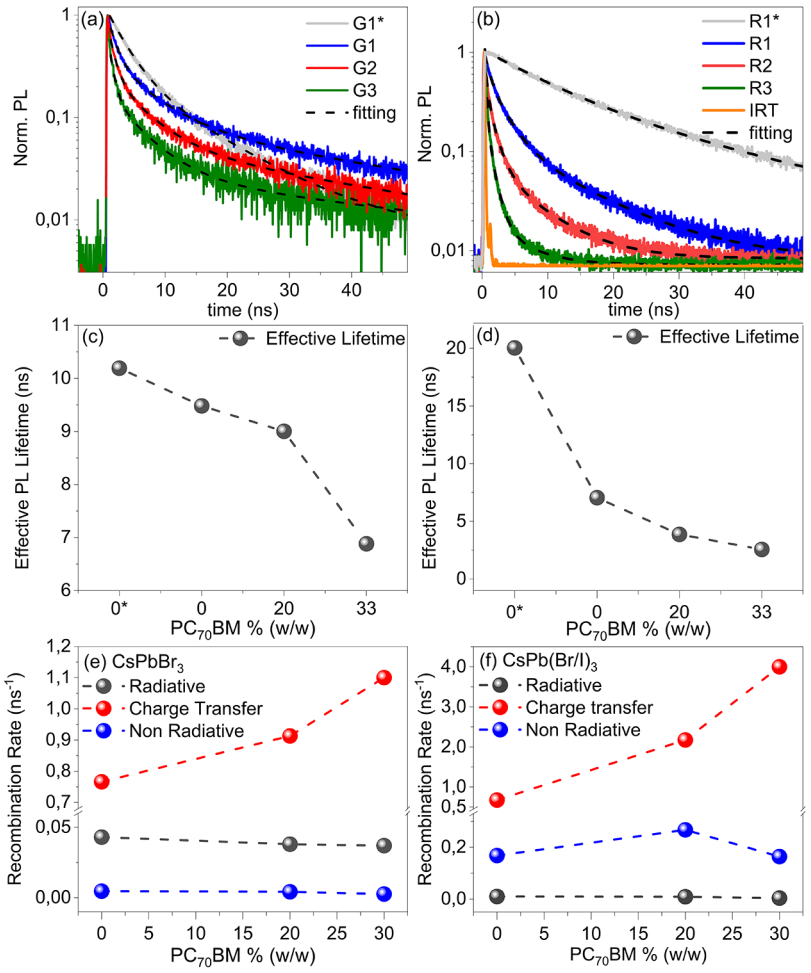

Figure 2. Time-resolved PL of samples containing (a) $CsPbBr_3$ and (b) $CsPb(Br,I)_3$ NCs. The orange spectrum in (b) shows the system response (IRT) that includes the excitation pulse shape. The effective PL lifetimes in each case are plotted in graphs (c,d) respectively. (e,f) Recombination rates (ns^{-1}) of each channel for (e) $CsPbBr_3$- and (f) $CsPb(Br,I)_3$-based films.

for the $CsPbBr_3$ (G1, G2, G3) and $CsPb(Br,I)_3$ (R1, R2, R3) NC-based films, respectively. A weak emission contribution from $PC_{70}BM$ in the 700−850 nm range is also observable, superimposed to the long wavelength tail of the $CsPb(Br,I)_3$ NC PL (Figure 1d). The emission can also be observed in the $CsPbBr_3$-based NC samples (G2, G3), as seen in the extended wavelength PL spectra of Figure S3. Similar emission quenching was observed in the two-sample series with slightly larger values in the green emitting blends of ∼79% (G2) and ∼92% (G3) compared to the ∼71% (R2) and ∼86% (R3) values in the red emitting samples.

Insight into the mechanisms of the emission quenching is provided by time-resolved PL experiments, with representative decays displayed in Figure 2a,b. In consistency with the steady-state PL results, addition of the $PC_{70}BM$ results in substantial shortening of the PL dynamics. To quantify the effect, the PL transients were fitted by multiexponential models. The decays of the nonwashed samples (G1*, R1*) can be well approximated with double exponentials, while triple exponentials were required to model the rest of the PL transients. As expected, the PL lifetime of the unprocessed mixed halide NC film (R1*) is significantly longer compared to the respective dynamics of the $CsPbBr_3$ NC (G1*) sample because of the increased dielectric screening[25] and exciton trapping at the disordered electronic landscape of the mixed halide NCs.[20] The results of the fits are summarized in Table 2, where $\tau_{1,2,3}$ are the time constants and $A_{1,2,3}$ is the relative amplitude of each decay channel, with the latter normalized for each decay based on the condition

$$\sum_i A_i = 1 \tag{2}$$

An initial evaluation of the PL dynamics can be obtained using the effective PL lifetime, computed based on the following equation[23]

Table 2. Multi-Exponential Fitting Results of the PL Decays

Fitting Results	$CsPbBr_3$ NC-based films				$CsPb(Br,I)_3$ NC-based films			
	G1*	G1	G2	G3	R1*	R1	R2	R3
A_1	0.65	0.23	0.20	0.19	0.31	0.11	0.06	0.02
τ_1 (ns)	5.0	5.3	5.2	5.1	28.0	11.0	6.5	5.3
A_2	0.35	0.08	0.07	0.04	0.69	0.42	0.32	0.18
τ_2 (ns)	13.7	17.1	16.6	15.2	9.50	2.5	1.2	1.1
A_3		0.69	0.73	0.77		0.47	0.62	0.80
τ_3 (ns)		0.9	0.8	0.7		0.7	0.3	0.2

https://doi.org/10.1021/acs.jpcc.3c07761
J. Phys. Chem. C 2024, 128, 5947−5955

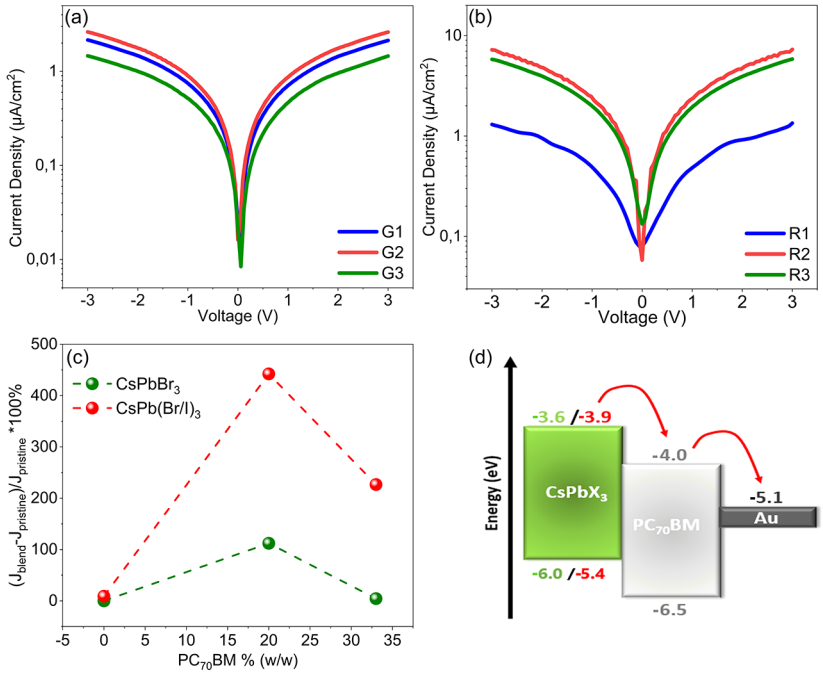

Figure 3. Photocurrent density versus voltage in the −3 to +3 V range collected by Au contacts for $CsPbBr_3$ NCs (a) and $CsPb(Br,I)_3$ (b). Photocurrent density enhancement ($\Delta J/J$) of $CsPbBr_3$ NC (green) and $CsPb(Br,I)_3$ NC (red) blend structure devices at the highest bias of 3 V (c). Schematic illustration of the energetic band alignment in the blend devices (d).

$$\tau_{\text{eff}} = \frac{\Sigma_i A_i \tau_i^2}{\Sigma_i A_i \tau_i} \tag{3}$$

The dependence of τ_{eff} on the $PC_{70}BM$ content is shown in Figure 2c,d. It can be observed that the lead acetate washing step has an impact on the PL dynamics of the pristine NC films, resulting in a reduction by ∼10% (∼65%) of the τ_{eff} of the $CsPbBr_3$ ($CsPb(Br,I)_3$) NCs.

Incorporation of $PC_{70}BM$ results in further quenching of the lifetime in both types of blend films. Analysis of the individual PL decay fitting parameters shown in Table 2 provides further insight into the mechanism of exciton recombination in the studied samples. The analysis is facilitated by computing the effective recombination rate, K_j for each of the three channels of the exponential fit model. The effective rate is defined by eq 4,[24] and displayed in Figure 2e,f for the two sample types

$$K_j = \frac{A_j}{\tau_j} \tag{4}$$

For the $CsPbBr_3$ NC-based films, the decay channel of 5 to 6 ns, appearing in all pristine and blend NC films, is attributed to radiative recombination. The assignment is based on the consistency of the observed decay constants with the typical range of radiative lifetimes reported in the literature for ensembles of $CsPbBr_3$ NCs in the solid state.[2] In addition, the channel is found to dominate the PL decay of the unprocessed NC film (G1*) with a relative amplitude of 65%, as expected for the radiative recombination of the efficient $CsPbBr_3$ NC emitters.[1−3] The channel contribution reduces upon treatment with the lead acetate and further diminishes as $PC_{70}BM$ is added due to exciton quenching at the NC:$PC_{70}BM$ heterointerfaces that competes with radiative recombination. For the $CsPb(Br,I)_3$ NCs, a much wider scattering in radiative lifetime values exists in the literature, as exciton properties are dependent on the method of anion exchange, the obtained Br to I relative ratio, and the extent of halide segregation in the film. The assignment of the radiative lifetime to the channel τ_1, as shown in Table 2, was based on the fact that such red-emitting NCs exhibit appreciable but overall, quite smaller emission QYs and concomitantly lower radiative rates (longer PL lifetimes) compared to $CsPbBr_3$ NCs.

A notable difference in the PL dynamics of the nonwashed pristine NCs versus the washed NC and blend films is that a third exponential channel (τ_3, A_3) is required to adequately reproduce the PL transients of the latter samples. The additional decay has dynamics in the sub-nanosecond to 1 ns range, and its relative weight increases rapidly as $PC_{70}BM$ is added into the films. As a result, it dominates the blend PL decay, effectively reducing the PL lifetime of the blends with respect to the two pristine G1* and R1* films. To interpret the origin of the decay, device data discussed in detail later on are used. Pristine $CsPbBr_3$ and $CsPb(Br,I)_3$ NC solids, not subjected to any washing treatment, were found to be insulating, as evidenced by the negligible photoconductance they exhibit. Even though such NCs are decorated by short octylamine and octanoic-acid ligands, synthesis results in excess ligands and byproducts that render such NC solids nonconductive in the mesoscopic, i.e., 50 μm, transport regime of the studied devices. The photoconductance is enhanced upon the mild washing treatment of the NCs and further increases upon addition of $PC_{70}BM$ in consistency with the respective increase of the τ_3 decay channel amplitude. Based on the above, a correlation of electrical conductivity with the presence and strength of the fast PL decay channel appears to exist. The channel is absent in untreated NC films in which conductivity diminishes and increases in a similar fashion to conductivity, as films become more purified and electronic doping by the fullerene acceptor is achieved. Based on the reported energetic alignment between the $CsPbBr_3$ NCs and

https://doi.org/10.1021/acs.jpcc.3c07761
J. Phys. Chem. C 2024, 128, 5947−5955

$PC_{70}BM$,[13] a conduction band offset of the order of ∼0.4 eV exists, favoring exciton dissociation via electron transfer to the fullerene. For $CsPb(Br,I)_3$ NCs, the offset is expected to be slightly reduced, but most probably the energetics still favor the electron-transfer processes. Based on the above, the third fast PL recombination channel is assigned to NC−NC and NC-$PC_{70}BM$ carrier transfer processes, enabling carrier transport in the treated NC pristine and blend films.

Following the assignment of the τ_1 and τ_3 to the radiative and the carrier transfer processes, the remaining channel τ_2 is naturally attributed to NC exciton nonradiative recombination. The interpretation appears to be consistent with the nature of exciton recombination in the two NC types. For $CsPbBr_3$ NCs, intrinsic recombination is dominated by the radiative term, as elaborated earlier, which is compatible with the significantly smaller amplitude and much longer τ_2 values compared to the respected parameters of the radiative term. The opposite trend is observed in the mixed halide NCs, where emission QY drops and the nonradiative (τ_2) and charge-transfer (τ_3) channels compete favorably to the radiative decay (τ_1) due to a smaller exciton binding energy and higher mobilities of electron and holes, respectively.

The spectroscopy findings provide strong evidence of efficient NC exciton quenching at the NC-fullerene heterointerface. The transient PL data further hint that such interfacial exciton dissociation results in electron transfer from the NC to the $PC_{70}BM$ blend phase. The combined process of exciton dissociation, charge transfer, transport, and extraction is evaluated in two-terminal, lateral, photoconductive devices based on interdigitated Au contacts bridged by 50 μm NC or NC:$PC_{70}BM$ channels. The device architecture allows for facile evaluation of the photoconductance, without the complication of interlayer(s) deposition and optimization. The simplicity in the device geometry comes at the expense of small device photocurrent densities at the level of few μA cm^{-2}, as the carrier diffusion lengths in such NCs are significantly smaller[13] compared to the 50 μm conductive channel length used.

The photocurrent was monitored while ramping the voltage in the range of −3 to +3 V. Under dark conditions, no conductance was measured. Upon illumination at 405 nm, semiconducting-like $I-V$s were obtained, with representative results for $CsPbBr_3$ and $CsPb(Br,I)_3$ NC-based devices, as shown in Figure 3a,b, respectively. In all devices, the dark current across the same bias range is negligible, as seen in Figure S4. To better quantify the impact of the fullerene additive on the conductivity, the relative change in the photocurrent density was used as a figure of merit, defined by the equation

$$\frac{\Delta J}{J} = \frac{(J_{blend} - J_{NC})}{J_{NC}} \times 100\% \quad (5)$$

where J_{blend} and J_{NC} are the average photocurrent density values measured for the respective blend and pristine NC device. The variation of $\Delta J/J$ for a maximum bias of 3 V is shown in Figure 3c. For the $CsPbBr_3$ NC-based devices, the addition of 20% w/w $PC_{70}BM$ in sample G2 results in a photoconductivity increase by 1 order of magnitude; however, further increase of the fullerene acceptor quenches the photocurrent at the level of the pristine NC device. For the mixed halide-based NC devices, an even greater improvement by as much as 4.5 orders of magnitude is obtained; higher $PC_{70}BM$ loading also results in reduction of photocurrent; however the 33% $PC_{70}BM$ blend produces still an appreciably larger photoresponse compared to the pristine NC device. The substantial photocurrent improvement observed in the blend devices overall indicates that the $PC_{70}BM$ phase acts as an efficient electron acceptor and transporter, effectively promoting electron-transfer cascade from the NCs to the $PC_{70}BM$ and finally to the Au contacts, as illustrated in the schematic of Figure 3d. The energy levels and band alignment illustrated in the figure were adopted by the reported work for $CsPbBr_3$ NC:$PC_{70}BM$[13] and $CsPb(Br,I)_3$ NCs[20] with NC sizes and compositions very similar to the respective NCs in our study.

The main difference between the spectroscopy and device data is that the former indicates a monotonic beneficial effect of the $PC_{70}BM$ content on exciton dissociation up to the maximum probed ratio of 33% w/w (samples G3, R3), while the devices' photoresponse is optimized for an intermediate concentration of 20% w/w $PC_{70}BM$ (G2, R2), in full agreement with the work by Yao et al.[13] Further increase of the fullerene content at a level of 50% w/w increases the NC emission quenching further but at the same time results in negligible device photocurrent. The apparent controversy can be attributed to the fact that devices evaluate the combined processes of (i) interfacial exciton dissociation, (ii) electron transfer from the NCs to $PC_{70}BM$, (iii) charge percolation through the NC and $PC_{70}BM$ phases, and (iv) charge collection by the contacts, while PL spectroscopy probes only the processes (i) and (ii). The negative impact on the device performance of the high fullerene loading can be attributed to various factors that include blocking of hole extraction by the $PC_{70}BM$ domains[13] and nonoptimum blending of the fullerene and the NCs. Hole blocking is a result of the deeper highest occupied molecular orbital level of $PC_{70}BM$ lying at ∼6.5 eV, compared to ∼6.0 eV for the green-emitting NCs and ∼5.7 eV for the red-emitting NCs. It is not clear how the morphology changes as the relative content of $PC_{70}BM$ increases. It is reasonable to assume that more $PC_{70}BM$ will result in more extended fullerene aggregation, as hinted by the substantial increase of light scattering in the absorption spectra of Figure 1. Increased aggregation can result in a larger phase separation between the NCs and fullerene domains. In such cases, charge extraction and collection can be improved, increasing the photocurrent, but this can be overcompensated by the decrease in heterointerfacial area that can reduce the exciton dissociation efficiency. Such reduction in interfacial quenching of the exciton is not consistent though with the trends of the PL study that show a monotonic increase of emission quenching with $PC_{70}BM$ in both the steady-state and the transient regime. The reduced photocurrent and increased emission quenching at high fullerene load instead seem more compatible with increased intermixing of the two phases, leading to a larger interfacial area but less optimum charge percolation, reducing the photocurrent. A comprehensive morphological investigation would be needed to further confirm such hypothesis and fully unravel the impact of the relative NC:$PC_{70}BM$ on the blend microstructure. Such a detailed structure−property study is beyond the scope of the presented work. Instead, an optical microscopy study was performed to probe the microstructure of the NC-fullerene blends in the mesoscopic regime, relevant to our studied device channel length i.e. ∼50 μm. The results of the study are contained in Figures S5 and S6. The data provide evidence of the formation of $PC_{70}BM$ clusters that are

https://doi.org/10.1021/acs.jpcc.3c07761
J. Phys. Chem. C 2024, 128, 5947−5955

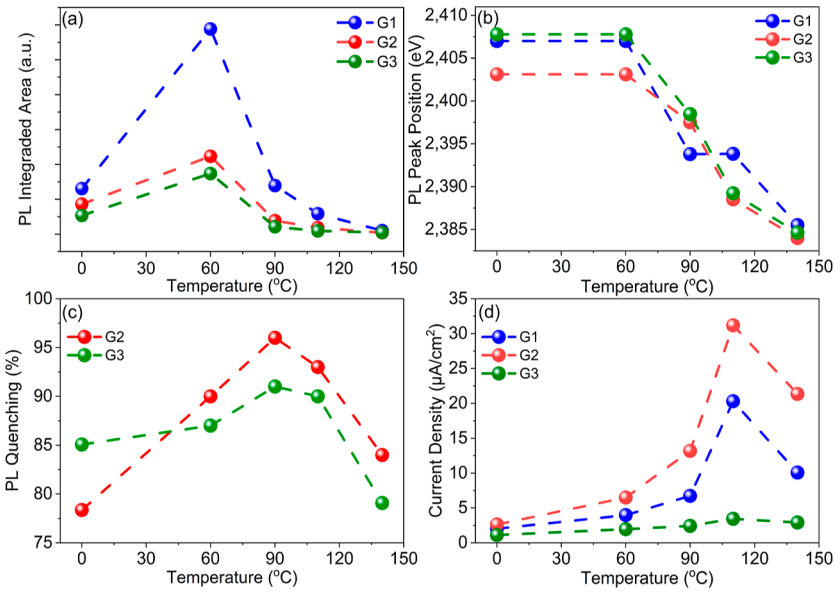

Figure 4. (a) Integrated PL area of pristine $CsPbBr_3$ NC and NC:$PC_{70}BM$ samples annealed at 4 different temperatures (60, 90, 110, and 140 °C), (b) evolution of PL peak position with annealing temperature, (c) PL quenching as a function of annealing temperature, and (d) photocurrent density at bias of 3 V as a function of annealing temperature.

smaller in size but appear better connected for the intermediate 20% w/w fullerene content compared to larger but more isolated fullerene aggregates of the film containing 33% w/w $PC_{70}BM$. Such result seems to support the hypothesis stated above based on which increase of the fullerene content suppresses the photocurrent due to a nonoptimum charge percolation within blends. More qualitative investigation of the influence of morphology is conducted by imposing the blend films and devices to a short thermal annealing, postfabrication step.

Thermal annealing treatment has been routinely used in OPVs to modify the microstructure and finely tune heterojunction phase domains within the scale of the exciton diffusion length for optimum charge separation.[21] Further to this, annealing has been employed to improve the homogeneity and optical quality of both NC[22] and perovskite[23] films, suppressing pinholes and voids, improving interfaces and grain boundaries, removing ligands and overall boosting the transport properties. The study was performed only on the pure $CsPbBr_3$ NC-based samples, as the mixed halide NCs were prone to degradation upon heating. The evolution of the PL integrated area with annealing temperature is displayed in Figure 4a with emission being optimized upon annealing at 60 °C as observed in Figure S7. For higher temperatures, PL quenches and red-shifts, as seen in Figure 4b, indicating extended NC aggregation. In terms of the fullerene-induced PL quenching, annealing appears beneficial up to 110 °C, as illustrated in Figure 4c. As hypothesized earlier, the PL quenching trend is most probably a consequence of better material mixing, which results in an increase of the interfacial area, improving further the NC exciton dissociation efficiency. In consistency with the PL results, the highest photo response is obtained by the intermediate $PC_{70}BM$ content of 20% w/w (G2) when imposed to 110 °C annealing, as seen in Figure 4d. Overall, the postfabrication, thermal treatment appears beneficial for the exciton dissociation and charge extraction in both films and devices.

The light to current conversion efficiency in the presented devices was obtained by estimating the responsivity R defined as the ratio of the photocurrent to the incident light intensity. The responsivity was calculated using the following equation

$$R = \frac{J_{ph}}{I_{light}} \tag{6}$$

where J_{ph} is the photocurrent density at 3 V and I_{light} is the incident excitation density of the 405 nm laser at 32 mW.

The estimated responsivity of the devices is shown in Table S1, with a maximum responsivity of ~8×10^{-5} and ~23×10^{-5} A/W for the $CsPbBr_3$-and the $CsPb(Br,I)_3$ NC-based samples, respectively. Upon thermal annealing, responsivity can be increased by 1 order of magnitude for the green-absorbing devices, reaching the level of 10^{-3} A/W, as observed in Table S2. The responsivity appears small, i.e., 2−3 orders of magnitude smaller than the respected values reported in the $CsPbBr_3$ NC:$PC_{70}BM$ photoconductive devices of ref 13. However, this variation merely reflects the respected large contrast between the ~50 μm channel length in our adopted lateral device geometry versus the ~50 nm active region thickness of the vertical devices of ref 13.

CONCLUSIONS

The optoelectronic properties of hybrid blends of green-emitting $CsPbBr_3$ or red-emitting mixed halide $CsPb(Br,I)_3$ NCs with the fullerene derivative $PC_{70}BM$ were examined to explore their potential for light harvesting applications. A simple synthetic protocol allowed the ambient production of perovskite NCs decorated by short octylamine and octanoic-acid ligands. The NCs form conductive solids upon mild postdeposition washing in the solid state, circumventing the need for more elaborate chemical ligand removal reactions performed at a controlled environment. The study demonstrates that the electronic properties of such NC films can be further and substantially improved via the addition of $PC_{70}BM$. In particular, the efficient suppression of the luminescence in

https://doi.org/10.1021/acs.jpcc.3c07761
J. Phys. Chem. C 2024, 128, 5947−5955

both the steady-state and transient regime provides strong evidence of efficient NC exciton quenching at the NC-fullerene heterointerface. A detailed analysis of the time-resolved PL data indicates the presence of three decay channels identified as the radiative, intrinsic nonradiative, and interfacial recombination of the NC exciton. As $PC_{70}BM$ increases, interfacial exciton dissociation prevails, and the transient decays become dominated by a fast, subnanosecond channel assigned to electron transfer from the NCs to the $PC_{70}BM$ blend phase. The electro-optical properties of the samples are evaluated via the fabrication and characterization of lateral photoconductive devices based on interdigitated Au contacts. Upon blending the NCs with the $PC_{70}BM$, an appreciable increase of the photoconductivity of such devices by up to 1 and 4 orders of magnitude, is observed for the $CsPbBr_3$ and $CsPb(Br,I)_3$ NC-based blends, respectively. Unlike the spectroscopic measurements that indicate a monotonic improvement of the exciton dissociation and the charge transfer process with the fullerene content, device data clearly show that the photoresponse is optimized for the intermediate concentration of 20% w/w of $PC_{70}BM$ for both green and red NCs. Based on our experiments, charge extraction at high fullerene loading is limited by blocking of hole extraction by the $PC_{70}BM$ and nonoptimum blending of the fullerene and the NCs. The photoconductivity properties of the blends can be further improved via postdeposition, thermal annealing with optimum annealing temperatures of the order of 100 °C. It is hypothesized that annealing improves both the homogeneity of the films as well as the heterointerface and mixing of the NC and fullerene phases. The facile, room-temperature synthesis, and processing of such blends, combined with their good electronic and photoconductive properties, makes them promising for solution-processable, light harvesting applications.

■ ASSOCIATED CONTENT

Supporting Information

The Supporting Information is available free of charge at https://pubs.acs.org/doi/10.1021/acs.jpcc.3c07761.

Optimization of device active region; optical microscopy images of the interpenetrated Au contact device; extended wavelength range PL spectra from the $CsPbBr_3$ (G1, G2, and G3) NC-based films; dark current I/Vs from all studied samples; optical and fluorescence microscopy images of the G2 and G3 samples; size distribution of $PC_{70}BM$ agglomerations; comparative PL intensity spectra of Br-based blend films subsequent to thermal annealing treatment at 60, 90, 110, and 140 °C; and responsivity of the devices (PDF)

■ AUTHOR INFORMATION

Corresponding Author

Grigorios Itskos − *Experimental Condensed Matter Physics Laboratory, Department of Physics, University of Cyprus, Nicosia 1678, Cyprus;* orcid.org/0000-0003-3971-3801; Email: itskos@ucy.ac.cy

Authors

Eleftheria Charalambous − *Experimental Condensed Matter Physics Laboratory, Department of Physics, University of Cyprus, Nicosia 1678, Cyprus; Inorganic Nanocrystals Laboratory, Department of Chemistry, University of Cyprus, Nicosia 1678, Cyprus*

Paris G. Papagiorgis − *Experimental Condensed Matter Physics Laboratory, Department of Physics, University of Cyprus, Nicosia 1678, Cyprus;* orcid.org/0000-0002-6627-0463

Nefeli Polycarpou − *Inorganic Nanocrystals Laboratory, Department of Chemistry, University of Cyprus, Nicosia 1678, Cyprus*

Fedros Galatopoulos − *Molecular Electronics and Photonics Research Unit, Department of Mechanical Engineering and Materials Science and Engineering, Cyprus University of Technology, Limassol 3603, Cyprus*

Apostolos Ioakeimidis − *Molecular Electronics and Photonics Research Unit, Department of Mechanical Engineering and Materials Science and Engineering, Cyprus University of Technology, Limassol 3603, Cyprus;* orcid.org/0000-0003-3974-6574

Stelios Choulis − *Molecular Electronics and Photonics Research Unit, Department of Mechanical Engineering and Materials Science and Engineering, Cyprus University of Technology, Limassol 3603, Cyprus;* orcid.org/0000-0002-7899-6296

Sotirios Christodoulou − *Inorganic Nanocrystals Laboratory, Department of Chemistry, University of Cyprus, Nicosia 1678, Cyprus;* orcid.org/0000-0001-7020-3661

Complete contact information is available at: https://pubs.acs.org/10.1021/acs.jpcc.3c07761

Notes

The authors declare no competing financial interest.

■ ACKNOWLEDGMENTS

This work was financially supported by the Research and Innovation Foundation of Cyprus under the "New Strategic Infrastructure Units-Young Scientists" Program (Grant Agreement no. "INFRASTRUCTURES/1216/0004," Acronym "NANOSONICS"). E.C.

■ REFERENCES

(1) Akkerman, Q. A.; Rainò, G.; Kovalenko, M. V.; Manna, L. Genesis, challenges and opportunities for colloidal lead halide perovskite nanocrystals. *Nat. Mater.* **2018**, *17*, 394−405.

(2) Dey, A.; Ye, J.; De, A.; Debroye, E.; Ha, S. K.; Bladt, E.; Kshirsagar, A. S.; Wang, Z.; Yin, J.; Wang, Y.; et al. State of the Art and Prospects for Halide Perovskite Nanocrystals. *ACS Nano* **2021**, *15*, 10775−10981.

(3) Kovalenko, M. V.; Protesescu, L.; Bodnarchuk, M. I. Properties and potential optoelectronic applications of lead halide perovskite nanocrystals. *Science* **2017**, *358*, 745−750.

(4) Li, M.; Bhaumik, S.; Goh, T. W.; Kumar, M. S.; Yantara, N.; Gratzel, M.; Mhaisalkar, S.; Mathews, N.; Sum, T. C. Slow Cooling and Highly Efficient Extraction of Hot Carriers in Colloidal Perovskite Nanocrystals. *Nat. Commun.* **2017**, *8*, 14350.

(5) Papagiorgis, P.; Protesescu, L.; Kovalenko, M. V.; Othonos, A.; Itskos, G. Long-Lived Hot Carriers in Formamidinium Lead Iodide Nanocrystals. *J. Phys. Chem. C* **2017**, *121*, 12434−12440.

(6) Li, M.; Begum, R.; Fu, J.; Xu, Q.; Koh, T. M.; Veldhuis, S. A.; Gratzel, M.; Mathews, N.; Mhaisalkar, S.; Sum, T. C. Low threshold and efficient multiple exciton generation in halide perovskite nanocrystals. *Nat. Commun.* **2018**, *9*, 4197.

(7) Swarnkar, A.; Marshall, A. R.; Sanehira, E. M.; Chernomordik, B. D.; Moore, D. T.; Christians, J. A.; Chakrabarti, T.; Luther, J. M.

Quantum dot-induced phase stabilization of α-CsPbI3 perovskite for high-efficiency photovoltaics. *Science* **2016**, *354*, 92−95.
(8) Ling, X.; Zhou, S.; Yuan, J.; Shi, J.; Qian, Y.; Larson, B. W.; Zhao, Q.; Qin, C.; Li, F.; Shi, G.; et al. 14.1% CsPbI3 Perovskite Quantum Dot Solar Cells via Cesium Cation Passivation. *Adv. Energy Mater.* **2019**, *9*, 1900721.
(9) Zhao, Q.; Hazarika, A.; Chen, X.; Harvey, S. P.; Larson, B. W.; Teeter, G. R.; Liu, J.; Song, T.; Xiao, C.; Shaw, L.; et al. High Efficiency Perovskite Quantum Dot Solar Cells with Charge Separating Heterostructure. *Nat. Commun.* **2019**, *10*, 2842.
(10) Li, F.; Zhou, S.; Yuan, J.; Qin, C.; Yang, Y.; Shi, J.; Ling, X.; Li, Y.; Ma, W. Perovskite Quantum Dot Solar Cells with 15.6% Efficiency and Improved Stability Enabled by an α-$CsPbI_3$/$FAPbI_3$ Bilayer Structure. *ACS Energy Lett.* **2019**, *4* (11), 2571−2578.
(11) Hao, M.; Bai, Y.; Zeiske, S.; Ren, L.; Liu, J.; Yuan, Y.; Zarrabi, N.; Cheng, N.; Ghasemi, M.; Chen, P.; et al. Ligand-Assisted Cation-Exchange Engineering for High-Efficiency Colloidal $Cs_{1-x}FA_xPbI_3$ Quantum Dot Solar Cells with Reduced Phase Segregation. *Nat. Energy* **2020**, *5* (1), 79−88.
(12) Zhang, X.; Huang, H.; Ling, X.; Sun, J.; Jiang, X.; Wang, Y.; Xue, D.; Huang, L.; Chi, L.; Yuan, J.; et al. Homojunction Perovskite Quantum Dot Solar Cells with over 1 μm-Thick Photoactive Layer. *Adv. Mater.* **2022**, *34* (2), No. e2105977.
(13) Yao, E. P.; Bohn, B. J.; Tong, Y.; Huang, H.; Polavarapu, L.; Feldmann, J. Exciton Diffusion Lengths and Dissociation Rates in $CsPbBr_3$ Nanocrystal-Fullerene Composites: Layer-by-Layer versus Blend Structures. *Adv. Opt. Mater.* **2019**, *7*, 1801776.
(14) Soltani, R.; Puscher, B. M. D.; Katbab, A. A.; Levchuk, I.; Kazerouni, N.; Gasparini, N.; Camaioni, N.; Osvet, A.; Batentschuk, M.; Fink, R. H.; et al. Improved charge carrier dynamics in polymer/perovskite nanocrystal based hybrid ternary solar cells. *Phys. Chem. Chem. Phys.* **2018**, *20*, 23674−23683.
(15) Hu, L.; Zhao, Q.; Huang, S.; Zheng, J.; Guan, X.; Patterson, R.; Kim, J.; Shi, L.; Lin, C. H.; Lei, Q.; et al. Flexible and efficient perovskite quantum dot solar cells via hybrid interfacial architecture. *Nat. Commun.* **2021**, *12*, 466.
(16) Yuan, J.; Zhang, X.; Sun, J.; Patterson, R.; Yao, H.; Xue, D.; Wang, Y.; Ji, K.; Hu, L.; Huang, S.; et al. Hybrid Perovskite Quantum Dot/Non-Fullerene Molecule Solar Cells with Efficiency Over 15%. *Adv. Funct. Mater.* **2021**, *31* (27), 2101272.
(17) Li, T.; Liu, M.; Li, Q.; Chen, R.; Liu, X. Hybrid photodetector based on $CsPbBr_3$ perovskite nanocrystals and $PC_{71}BM$ fullerene derivative. *Chem. Phys. Lett.* **2018**, *699*, 208−211.
(18) Scalon, L.; Freitas, F. S.; Marques, F. d. C.; Nogueira, A. F. Tiny spots to light the future: advances in synthesis, properties, and application of perovskite nanocrystals in solar cells. *Nanoscale* **2023**, *15*, 907−941.
(19) Di Stasio, F.; Christodoulou, S.; Huo, N.; Konstantatos, G. Near-Unity Photoluminescence Quantum Yield in $CsPbBr_3$ Nanocrystal Solid-State Films via Postsynthesis Treatment with Lead Bromide. *Chem. Mater.* **2017**, *29*, 7663−7667.
(20) Christodoulou, S.; Di Stasio, F.; Pradhan, S.; Stavrinadis, A.; Konstantatos, G. High-Open-Circuit-Voltage Solar Cells Based on Bright Mixed-Halide $CsPbBrI_2$ Perovskite Nanocrystals Synthesized under Ambient Air Conditions. *J. Phys. Chem. C* **2018**, *122*, 7621−7626.
(21) Kippelen, B.; Brédas, J.-L. Organic photovoltaics. *Energy Environ. Sci.* **2009**, *2*, 251−261.
(22) Talapin, D. V.; Lee, J.-S.; Kovalenko, M. V.; Shevchenko, E. V. Prospects of colloidal nanocrystals for electronic and optoelectronic applications. *Chem. Rev.* **2010**, *110*, 389−458.
(23) Stranks, S. D.; Snaith, H. J. Metal-halide perovskites for photovoltaic and light-emitting devices. *Nat. Nanotechnol.* **2015**, *10*, 391−402.
(24) Patterson, J.; Bailey, B. Optical Properties of Solids. In *Solid-State Physics*; Springer, 2010, pp 545−590..
(25) Diroll, B. T.; Zhou, H.; Schaller, R. D. Low-Temperature Absorption, Photoluminescence, and Lifetime of $CsPbX_3$ (X = Cl, Br, I) Nanocrystals. *Adv. Funct. Mater.* **2018**, *28*, 1800945.

https://doi.org/10.1021/acs.jpcc.3c07761
J. Phys. Chem. C 2024, 128, 5947−5955